

Microstructural Characterization, Residual Stress, and Mechanical Properties of Plasma Sprayed 8YSZ Thermal Barrier Coatings

Nikhil Kadam^{a,*}, Ganesh Karthikeyan^a, Dhananjay Kulkarni^a, Prajakta Jagtap^b

^aBITS Pilani, K. K. Birla Goa Campus, NH17B Airport Road, Zuarinagar, Goa, India 403 726,

^bSanjivani Group of Institute, College of Engineering, Sanjivani, Kopergaon, Maharashtra, India 423 603.

Keywords:

Thermal barrier coatings
Atmospheric plasma spray
Spray angle
Microstructure
Porosity
Residual stress
Thermal conductivity
Hardness
Roughness

ABSTRACT

The plasma sprayed 8YSZ TBC is applied on a Ti-6Al-4V substrate with a NiCrAlY bond coat. The effect of spray angle on the coating microstructural, residual stresses, and mechanical properties is studied in the paper. The surface and cross-sectional coating structure were analyzed by scanning electron microscopy and elemental composition with energy-dispersive x-ray spectroscopy. The SEM image greyscale threshold determined the porosity level in the structure. The residual stresses and thermal conductivity were measured by Raman spectroscopy and laser flash technique. The mechanical property, such as hardness and surface roughness was determined using the indentation and surf test profilometer. The result showed that the spray angle affects the coating structure - grain size, shape and distribution, and mechanical properties. The P90 TBC showed a uniform and dense structure with avg. grain size of ~ 850nm, whereas P60 showed a non-uniform structure with avg. grain size of ~ 300nm. The 60° inclined spray angle leads to more defects such as cracks and pores than the 90° normal spray angle. In both surface and cross-sectional structures, the porosity level increases with a decrease in the spray angle conditions. The P90 TBC results in high compressive residual stresses than the P60 structured TBC. The avg. Raman shifts for P90 and P60 TBCs are $1.5667 \pm 1.022 \text{ cm}^{-1}$ and $1.3 \pm 0.973 \text{ cm}^{-1}$, respectively. The thermal conductivity decreases with increased porosity and low spray angle. The P90 showed better hardness and uniform surface than P60 TBC.

* Corresponding author:

Nikhil Kadam 
E-mail:
p20150410@goa.bits-pilani.ac.in

Received: 23 May 2021

Revised: 29 June 2021

Accepted: 22 July 2021

© 2022 Published by Faculty of Engineering

1. INTRODUCTION

Thermal Barrier Coatings (TBCs) development started in the 1950s for defense engines [1]. Later the TBCs were adopted in commercial services such as X-15 manned rocket exhaust nozzle, gas turbine, and aero engines [2-3]. The TBC consists of a

multilayer structure with a superalloy substrate, metallic bond coat, and ceramic topcoat. Figure 1 shows the TBC structure with different layered materials, its function with coating thickness. The metallic bond coat consists of MCrAlY (M-Ni/Co), providing an irregular surface to improve adhesion between the substrate and ceramic topcoat. It also

provides oxidation and corrosion protection with a reduction in the coefficient of thermal expansion. At high temperatures, the bond coat leads to thermally grown oxides acting as an oxidation barrier to the substrate. The ceramic topcoat provides thermal insulation protecting against high temperature forming the thermal barrier coating [4-5].

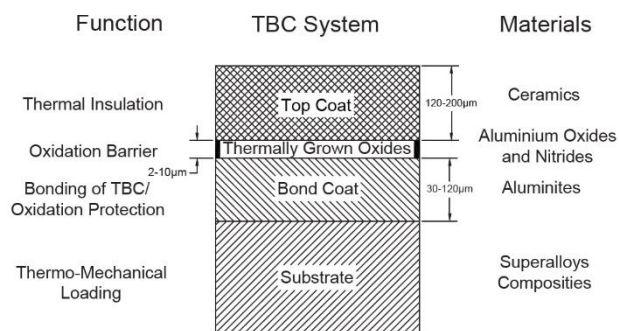


Fig. 1. Multilayer TBC structure [6].

Generally, the TBC is deposited by atmospheric plasma spray and electron beam physical vapour deposition. The coating deposition processes have various spraying parameters that influence the coating structure, properties, and quality. The few plasma spraying parameters such as spray angle, spray distance, substrate rotation, substrate temperature, powder feed rate, and carrier gas flow rate can be controlled to obtain a better TBC structure. Among the above spray parameters, the spray angle variation was considered for the comparative study. As a thumb rule, the normal spray angle is in the line of sight, i.e., perpendicular to the substrate to be coated. The deviation could result in compromising the coating properties. Generally, the spray angle for the low-velocity process must be within $\pm 15^\circ$ of normal, and high-velocity within $\pm 45^\circ$ [7]. Therefore, the high-velocity plasma spray can be considered 90° as normal spray angle and 60° as the middle level of tolerance from normal angles as lower spray angle could result in larger elongation with more wastage feedstock material [8]. It also leads to the porous structure, resulting in low hardness and a young's modulus increase in coating defects [9].

Ling et al. [10] investigated and found the dense coating structure with high hardness with short spray distance. Mantry et al. [11] and Kumar and Pandey [12] studied the different spraying parameters that affect the coating structure in roughness, thickness, and hardness. Morks et al. [13] and John et al. [14] investigated and found the influence of spraying parameter and multilayer

process, controlling the coating porosity with improvement in hardness value. Also, the rare earth addition and surface re-melting could lead to improvement in surface properties. Izadinia et al. [15] found the effect of the spraying parameter onto the conventional splat layer structure. The improved hardness and porosity can be controlled with few segmented cracks in the coating structure. Nayak et al. [16] studied the effect of coating thickness on plasma sprayed TBC and found improvement in the bond strength with the low value of the coating thickness. Wang et al. [17], Zhu and Ma [18], and Ekberg et al. [19] investigated and found that the feedstock, its spray parameters, and heat treatment could affect the coating structure and properties resulting in improvement. Zang et al. [20] and Ganvir et al. [21] found that the coating with a porous structure can decrease thermal conductivity. Teixeira et al. [22], Scrivani et al. [23] and Portinha et al. [24] investigated the TBC during thermal cycle to find the residual stresses developed. They found that as the substrate temperature was increased, the tensile stresses were change to compressive stresses resulting in the generation of considerable residual stress. Also, the increase in coating porosity could result in decreased value of residual stress. Based on the literature surveyed, it was clear that the spray parameters affect the coating structure, thermal and mechanical properties. Therefore, the variation in spray angle parameter was considered to find the effect on the coating structure, thermal and mechanical properties.

In the present work, the plasma sprayed 8YSZ TBCs were deposited onto the Ti-6Al-4V substrate with NiCrAlY bond coat. The effect of spray angle was studied to find the influence on the coating microstructure, porosity, residual stresses, and mechanical properties. First, the surface and cross-sectional coating structure were examined by scanning electron microscopy (SEM) and elemental composition with energy-dispersive x-ray spectroscopy (EDS). Then, the porosity level in the structure was determined using the SEM image analysis-grey scale threshold. Next, the thermal residual stresses and thermal conductivity were measured using Raman spectroscopy and laser flash technique. Finally, the mechanical property such as hardness and surface roughness was measured using indentation and surf test profilometer. Based on the experimental analysis, a discussion was made with the effect of spray angle on the microstructural characterization, residual stress, and mechanical properties.

2. EXPERIMENTATION

2.1 Substrate preparation

The titanium grade 5 alloy Ti-6Al-4V was procured in thin sheets with a thickness of 3 mm and was sectioned into the square-shaped 20×20 mm dimension. The single sheet was used to prepare the substrate to ensure the minimal composition variation among the substrate. The chemical composition of Ti-6Al-4V by wt. %: Al-5.7%, V-4.1%, Fe-0.2%, H-0.13%, O-0.1%, N-0.04%, Y-0.05%, Ti-bal was determined using spectroscopy analysis [25]. Before deposition, the substrate surface was grit blasted with alumina abrasive particle size 120µm and a flow rate of 2kg/min. The grit blasting pressure was varied from 2 to 3bar with an increment of 0.5bar at the stand-off distance of 100mm with a 45° spray angle [26-27]. Grit blasting aims to create adequate surface roughness to ensure better mechanical interlock and bonding between substrate and coating layer. After grit blasting, the substrate was cleaned with acetone and water using the ultrasonic technique for 30 min. and dried.

2.2 Coating material, deposition process, and its spray parameters

The NiCrAlY (Type: AMDRY 962) and 8 wt. % yttria-stabilized zirconia (Type: 204B-NS) feedstock manufactured by Sulzer Metco Inc. USA were used to deposit metallic bond coat and ceramic topcoat onto the Ti-6Al-4V substrate. The plasma sprayed process was used to deposit bond coat and top coat TBC with the variation of spray angle condition. The NiCrAlY bond coat was deposited considering standard spray parameters for both the samples, whereas 8YSZ were deposited with the variation of spray angle, i.e., 90° and 60°. The coating thickness for the NiCrAlY bond coat is $\pm 100\mu\text{m}$, whereas the 8YSZ TBCs were of $\pm 300\mu\text{m}$. The spraying parameters used to deposit TBCs are listed in Table 1. Figure 2 shows the plasma spray system 9MBM machine mount (Make: Sulzer Metco AG, Switzerland) with 40KW capacity and 6mm internal nozzle diameter. The plasma spray system is available at Spraymet Surface Technologies Pvt. Ltd., Bangalore, Karnataka, India.

The spray angle means the angle between the plasma gun and substrate material. The substrate is fixed, whereas the plasma gun is inclined as per the requirement. At a 90° spray angle, the plasma

gun and substrate were perpendicular, whereas the plasma gun was tilted at a 60° spray angle. In both cases, the spray distance was maintained constant to the substrate center point. At 90°, the whole upper surface had constant spray distance whereas, at 60°, the substrate center made the constant distance, with the left side upper and right lower than the center point positioned. Figure 3 shows the spray angle variation and spray angle direction. Figure 4 shows the plasma sprayed deposited 8YSZ TBCs with the variation of spray angle condition.

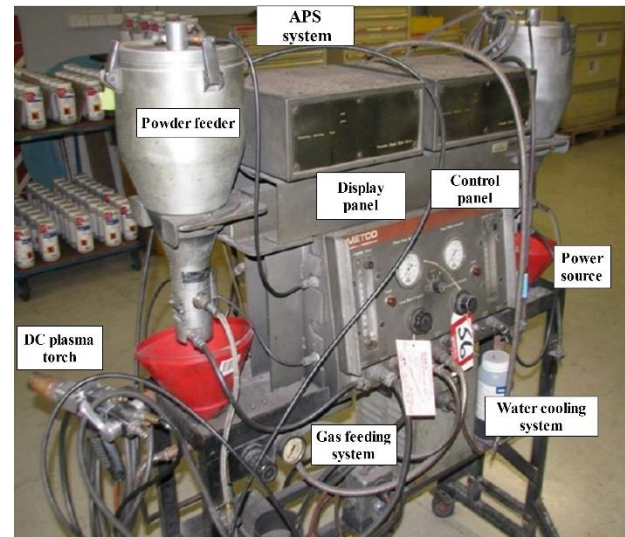


Fig. 2. APS system and accessories (Courtesy: Spraymet Surface Technologies Pvt. Ltd., Bangalore, Karnataka, India).

Table 1. Spray parameter to deposit plasma sprayed 8YSZ TBCs [6,26].

Process Parameter	Bond coat	Topcoat
Feedstock	NiCrAlY	8YSZ
Current (A)	400	500
Volatge (KV)	60	65
Primary gas flow rate – Ar (slpm)	100	80
Secondary gas flow rate – He (slpm)	5	15
Primary gas pressure – Ar (MPa)	0.69	
Secondary gas pressure – He (MPa)	0.35	
Powder feed rate (gm/min)	100	30
Particle velocity (m/sec)	≤ 450	
Substrate rotation	Stationary	
Spray distance (mm)	88.9	63.5
Spray angle (°)	90	60-90

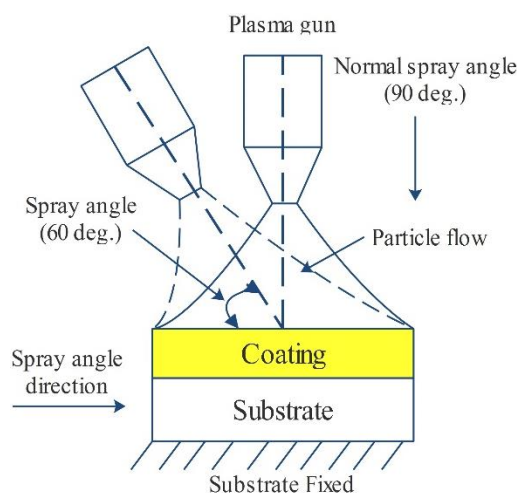


Fig. 3. Schematic diagram of spray angle variation and spray angle direction.

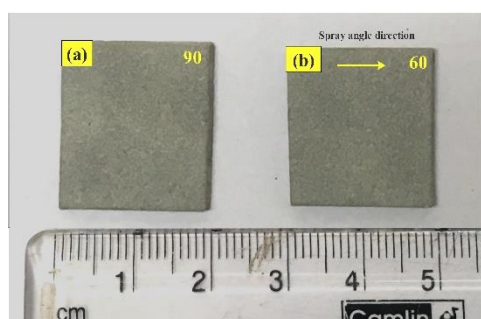


Fig. 4. Atmospheric plasma spray enabled 8YSZ TBCs with spray angles (a) 90° and (b) 60°.

2.3 Characterization

The elemental spectrum, phase composition, and microstructure examination of feedstock and coating microstructure were examined using SEM (Quanta FEG 250, Hillsboro, USA) with EDS. The surface and cross-sectional structure were examined with the variation of spray angle parameters. The electron beam was focused onto the feedstock and TBC with low accelerating voltage. The microstructural examination was observed to identify the surface characterization in terms of particle size, shape and distribution, the flow of particles, flatter of particles, and presence of defects through SEM. In addition, the EDS unit attached to SEM was used to identify the phase composition of the feedstock. As both the feedstock were non-conductive, the gold/palladium (Au/Pd) coating was applied using magnetron sputtering (Leica EM ACE200, Germany) to avoid charging with thermal damage reduction for improvement topographic imaging.

The porosity level in the coating structure was determined using SEM images with the greyscale

threshold technique [25-26,28-30]. The microstructure images obtained through SEM were cleaned with an RGB setting using ImageJ software. The scanned and cleaned coating structure images highlight the pores, cracks, and surface irregularities in the black portion and grain structure in the white portion. The total and porous areas were measured and repeated at different locations with an equal amount of accurate and precise analysis.

The residual stresses were determined by a Raman spectrometer (Lab Ram spectrometer, HORIBA Jobin Yvon, France) during thermal loading. The argon-ion laser with $\lambda=532\text{nm}$ wavelength and 5mW power was used as an excitation source. The dense surface coating structure was found and focused on through a 50 \times objective. The thermal loading cycle consists of heating, dwell, and cooling. During the heating cycle, the TBC was heated at 500°C for 10 mins. followed by a dwell of 10 mins and cooled at room temperature with a cooling rate of 50°C/min. In total, 15 thermal cycles were repeated, and the spectra after every five thermal cycles were recorded to find the relative amount of various phases.

The thermal conductivity (k) was measured by laser flash technique (Discovery laser flash DLF 1200, India). The thermal conductivity was made according to the procedure prescribed in ASTM E1461-11 [31]. One side of the TBC sample was heated using a short-duration laser pulse, and the infrared detector measured the other side's temperature. The thermal conductivity was measured up to 1000°C with an interval of 200°C. At every 200°C interval, the TBC sample was heated for the duration of 2 hrs. The thermal conductivity was measured by formula (1):

$$k = \alpha C_p \rho \quad (1)$$

where k - thermal conductivity, α - thermal diffusivity, C_p - specific heat, and ρ - coating density.

The coating hardness (Pa) was determined by quad shaped pyramid diamond indenter (Matsuzawa VMT-7, Japan) through a 40 \times objective. The 5kgf load with a dwell period of 10sec was applied. The hardness measurement was made according to the procedure prescribed in ASTM E92-82 [32] and ASTM E384-17 [33]. The hardness values obtained on each sample were recorded five times - one on the center and four on each corner.

The surface roughness (Ra) was measured by a surf test profilometer (Mitutoyo SJ 410, Japan) with a cut-off length of 8mm, probe trace speed of 0.5mm/sec, and measurement length of 16mm. The arithmetic mean roughness values obtained on each sample were scanned and recorded six times – three on X-direction and three on Y-direction with equal interval.

All the microstructural images and Raman spectrum were captured in the controlled temperature and mechanical properties at room temperature.

3. RESULT AND DISCUSSION

3.1 Surface morphology of feedstock

Figure 5 (a) and Figure 5 (b) show the feedstock morphology of NiCrAlY and 8YSZ. The magnified microstructure of NiCrAlY feedstock shows the solid spherical morphology with particle size ranging from 10 to 100µm, and 8YSZ feedstock shows hollow spherical morphology with particle sizes ranging from 5 to 60µm.

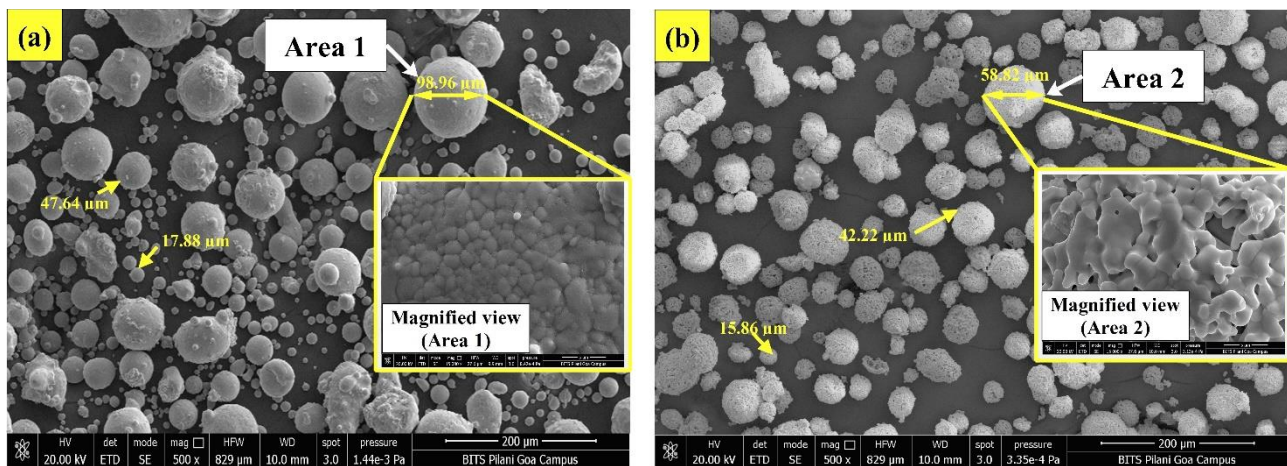


Fig. 5. Microstructure of (a) NiCrAlY and (b) 8YSZ feedstock [25].

3.2 Phase composition and elemental spectrum of feedstock

The elemental composition of the metallic bond coat and ceramic topcoat was determined by energy-dispersive x-ray spectroscopy (EDS) attached to the SEM facility. Figure 6 shows the elemental spectrum and phase composition by wt. % for NiCrAlY and 8YSZ feedstock for area 1 and area 2 (refer to Figure 5), respectively. The uniform presence of elemental composition was found throughout the feedstock. The uniformity in the feedstock elements and phase composition can result in

similar composition even after coating deposition. This helps to identify the impurity and presence of other elements, resulting in producing defects in the coating. From Figure 6, it was seen that the NiCrAlY feedstock results in a high amount of nickel, chromium, and aluminum with a small amount of carbon, oxygen, and yttrium by wt. %. The 8YSZ feedstock shows a high amount of zirconium, oxygen, and yttrium by wt. %. The presence of Au/Pd was not detected in the EDS spectrum as the amount of Au/Pd sputtering applied onto the feedstock was very minimal, with a coating thickness of ± 5 nm.

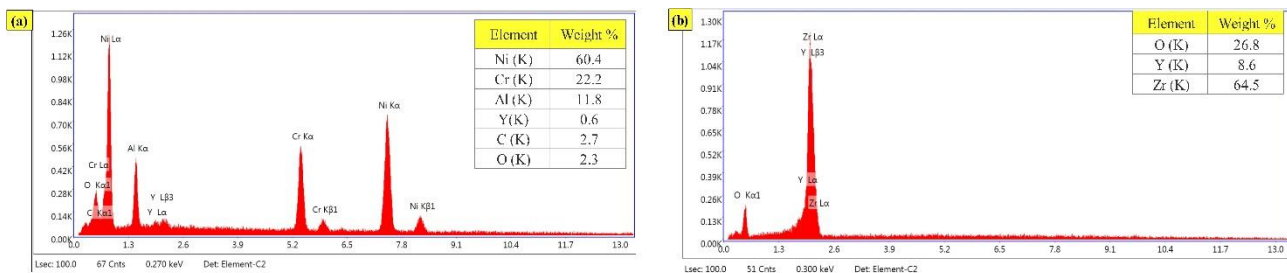


Fig. 6. EDS spectrum of feedstock (a) NiCrAlY (area 1) and (b) 8YSZ (area 2) as shown in Fig. 5 [25].

3.3 Surface morphology of NiCrAlY

The surface microstructure of NiCrAlY was examined and analyzed in terms of surface uniformity and particle distribution. Both the bond coat samples were deposited in a single set of spraying conditions to have an almost similar coating structure with minimal difference. Figure 7 showed NiCrAlY bond coat structure and its magnified view for microstructural examination. Figure 7 (a) clearly showed that the coating

structure was not uniform, and the presence of unmelted and partially melted particles was observed. Some amount of flatterings were seen with few defects present in the structure. However, the presence of defects such as pores and cracks were visible. Figure 7 (b) shows the magnified view of the structure to identify the shape of the pores, i.e., circular and irregular. Also, it sees the uniformity of the surface. The more the rough surface, the better adhesion between the ceramic coatings.

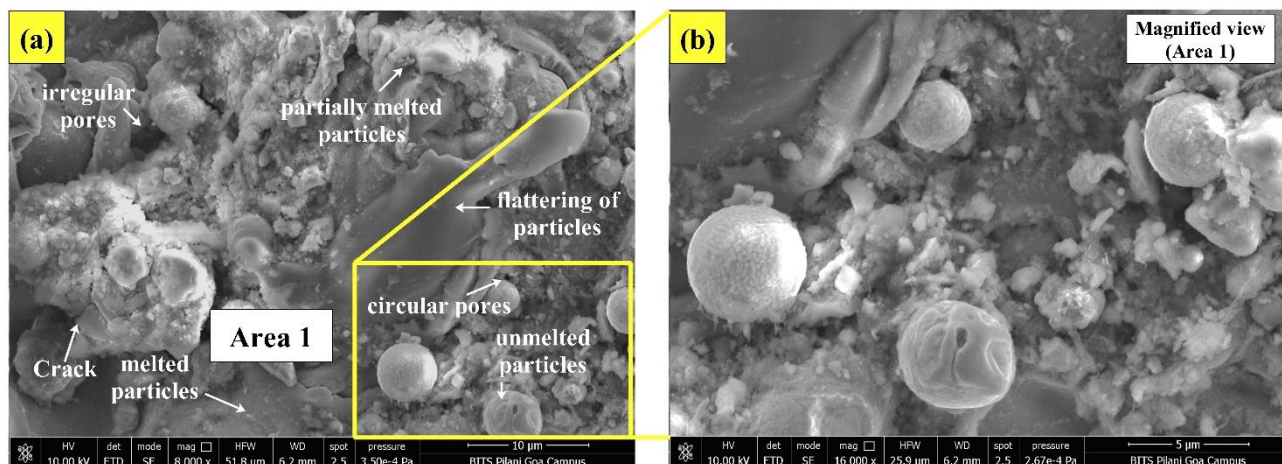


Fig. 7. (a) Surface microstructure of NiCrAlY bond coat by APS and (b) magnified view of area 1.

3.4 Surface morphology of 8YSZ TBCs

The surface microstructure of 8YSZ TBCs was examined with the variation of spray angle conditions. The microstructural characteristics were analyzed in terms of surface uniformity, grain structure, grain size, shape, and distribution with features such as melted particles, unmelted particles, flatterings of particles, and defects such as the network of cracks, pores, and voids. Both the samples were coated with NiCrAlY with similar spraying parameters using plasma spray in a single set with an equal number of spray passes. The spray angle variation, i.e., 90° and 60°, was used to deposit 8YSZ TBCs. The notation used for 90° and 60° spray angles were P90 and P60, respectively.

Figure 8 (a) and Figure 8 (b) show the plasma sprayed 8YSZ TBCs with a 90° spray angle with a magnified structure. The magnified P90 TBC structure showed a uniform and dense structure. The P90 TBC shows the grain structure with few unmelted particles and a network of cracks. The segmented cracks are visible, leading to crack branching. As the melted particles solidify quickly, which results in crack formation.

In both spraying conditions, pores and cracks are observed with different sizes, shapes, and distributions. The spray parameters can change the coating microstructure, resulting in different grain structure growth and defects [34]. The splat morphology, i.e., the splat elongation, is increased when the spray angle is decreased [8].

Figure 9 (a) and Figure 9 (b) show the plasma sprayed 8YSZ TBCs with a 60° spray angle and magnified view. As the inclined spray angle was considered, the P60 results in more splashing of molten particles onto the coating surface. This phenomenon results in more non-uniform surfaces with more defects. The magnified P60 TBC showed large crack width with a high crack angle, whereas the magnified P90 TBC showed small crack width with a small crack angle. Hexagonal structure grain boundaries with inter-crystalline space and equiaxed are observed in both spray angle conditions. The grain growth in P90 TBC was almost similar, whereas, in P60 TBC, the elongation in grain shape was observed in the spray angle direction. Considering the grain size, the P90 showed the average grain size of ~850nm, and P60 showed ~300nm. The coating area

exposed to pores, voids, and cracks leads to fast cooling resulting in a change in grain boundary structure leading to the brittle fracture. The spray angle parameter affects the coating

microstructure in terms of the molten flow of particles, presence of defects such as cracks and pores. It also affects the grain structure in terms of grain size, shape, and distribution.

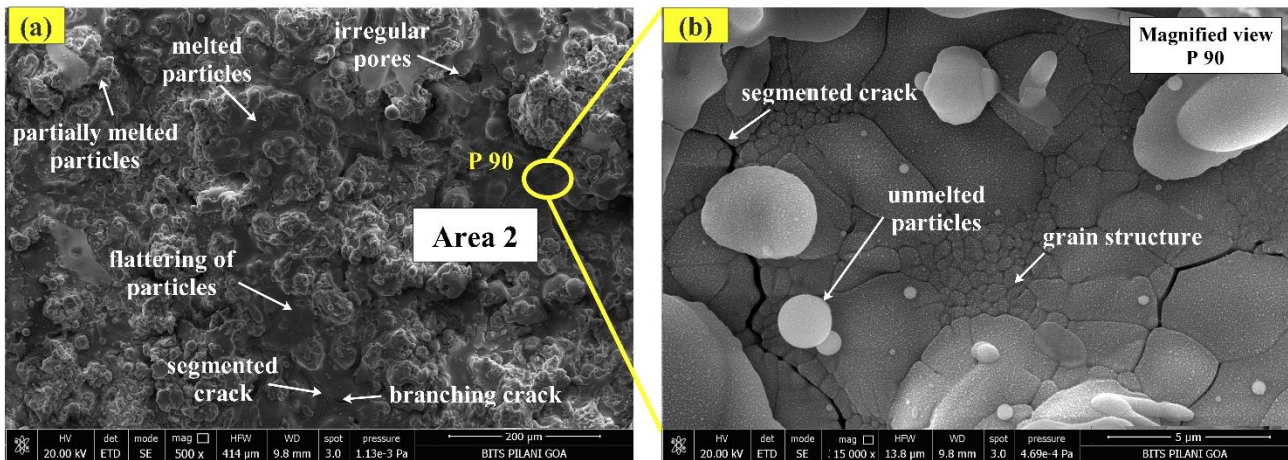


Fig. 8. (a) Surface microstructure of 8YSZ TBCs with 90° spray angle and (b) magnified view of area P90.

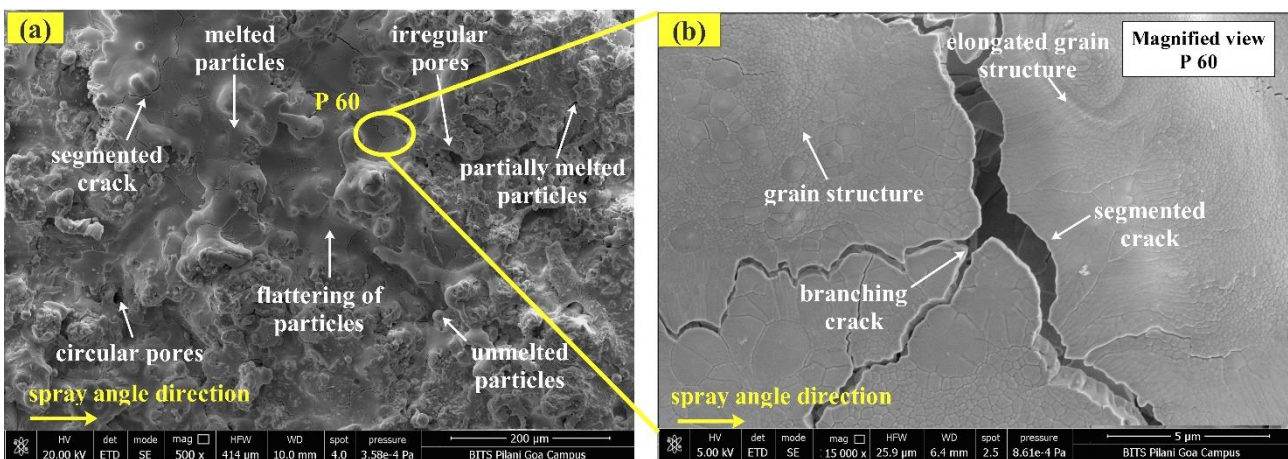


Fig. 9. (a) Surface microstructure of 8YSZ TBCs with 60° spray angle and (b) magnified view of area P60.

3.5 Cross-sectional morphology of 8YSZ TBCs

Figure 10 and Figure 11 show the cross-section structure with the variation of spray angle. Both the TBC sample showed Ti-6Al-4V substrate, metallic NiCrAlY bond coat, and ceramic 8YSZ top coat. Figure 10 (a) represents the coating structure with normal spray angle direction (perpendicular direction), and Figure 11 (a) represents with inclined spray angle direction. Both the cross-sectional structure were captured at high magnification to observe the different phenomena present in the coating structure. Figure 10 (b) and Figure 11 (b) showed the magnified structure representing grain structure, the network of cracks, pores, and unmelted regions. Both spray angles

showed a vertical grain growth structure, which shows a strong bond over the two splats. The P90 TBC showed a low amount of intra-splat and inter-splat crack at a higher magnification than that of the P60 sample. Also, the P90 had a small width crack compared to the P60 large width crack. Even the defects such as unmelted particles, pores, and cracks were in the large amount. Due to the poor adhesion between the splat structures, the inter-splat cracks are formed. Both coating structures had horizontal cracks that penetrate the surface, which could cause growth in a vertical crack. The vertical crack separates the splat layer structure, resulting in early spallation failure than a horizontal crack that runs through the dense structure [35].

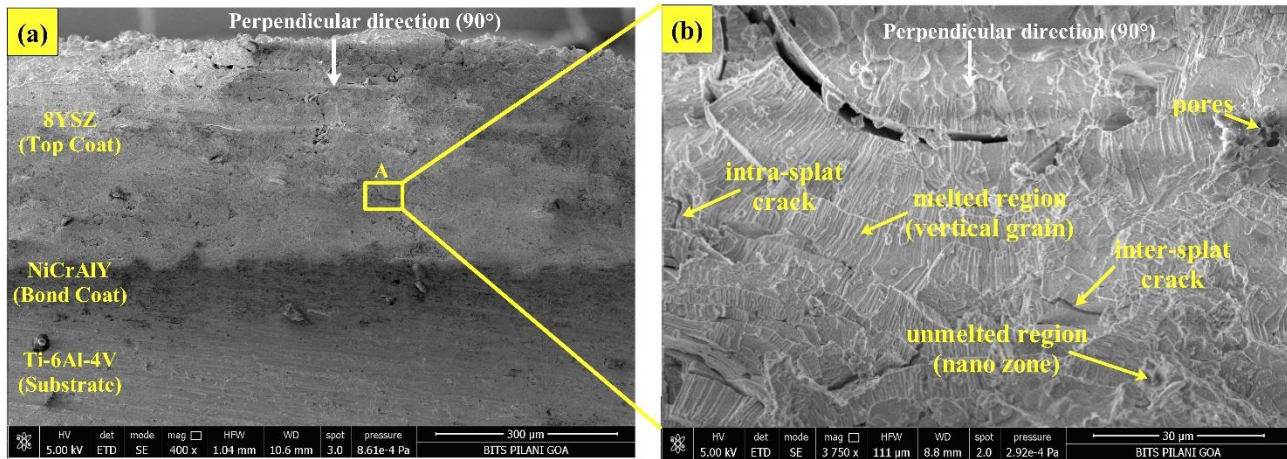


Fig. 10. (a) Cross-sectional microstructure of 8YSZ TBCs with 90° spray angle and (b) magnified view of area A.

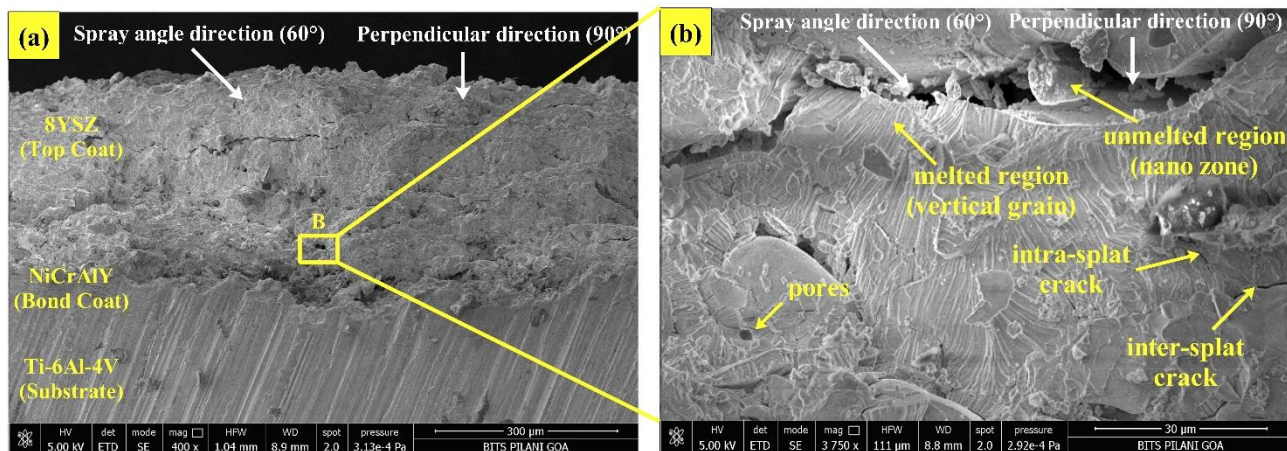


Fig. 11. (a) Cross-sectional microstructure of 8YSZ TBCs with 60° spray angle and (b) magnified view of area B.

3.6 Phase composition and elemental spectrum of TBCs

EDS determined the phase composition and elemental spectrum of NiCrAlY and 8YSZ TBCs. Figure 12 shows phase composition by wt. % and elemental spectrum for NiCrAlY coating (refer to

Figure 7-area 1) and 8YSZ coating (Figure 8-area 2). Figure 12 (a) shows that the NiCrAlY coating shows a high amount of nickel, chromium, and aluminum with a small amount of carbon, oxygen, and yttrium by wt. %. Similarly, Figure 12 (b) shows that the 8YSZ coating results in a high amount of zirconium, oxygen, and yttrium by wt. %.

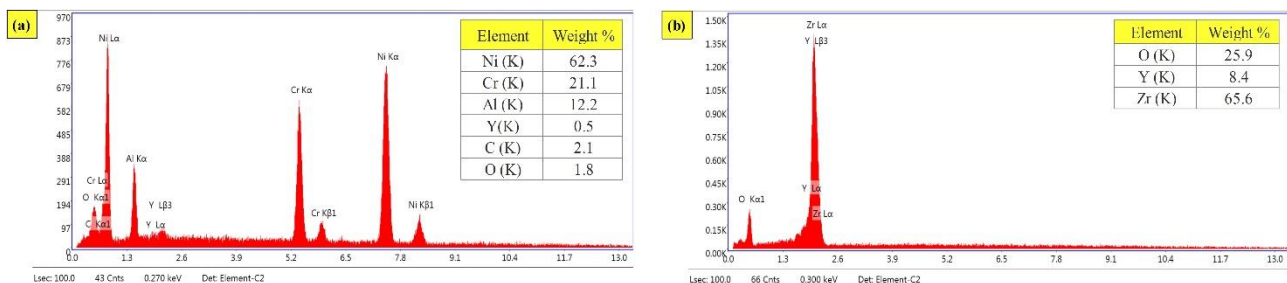


Fig. 12. EDS spectrum of coating structure (a) NiCrAlY (refer Figure 7-area 1) and (b) 8YSZ (Figure 8-area 2).

3.7 Porosity analysis

The 8YSZ TBC structure showed the porosity level in the wide range of cracks, pores, and

surface irregularities. The presence of unmelted and partially melted particles deposited onto the coating in low flatter conditions forms a porous structure. This

porous structure leads to a rough surface resulting in poor adhesion between particles of different coated layers. Microstructural images determined the porosity analysis at magnification (200×) with the greyscale threshold technique. The ImageJ software was used to process the binary image to single-channel RGB greyscale to represent pores and cracks in the coating. The noise present in the images was removed by split-channel for

processing in porosity analysis. The no noise or minimum noise image from the red band was considered. Figure 13 shows the surface porosity images generated by ImageJ with a single RGB greyscale threshold channel showing pores, cracks, and surface irregularities in the black portion and grains in the white portion. Figure 14 shows the cross-sectional porosity images of the 8YSZ layer with the variation of spray angle parameter.

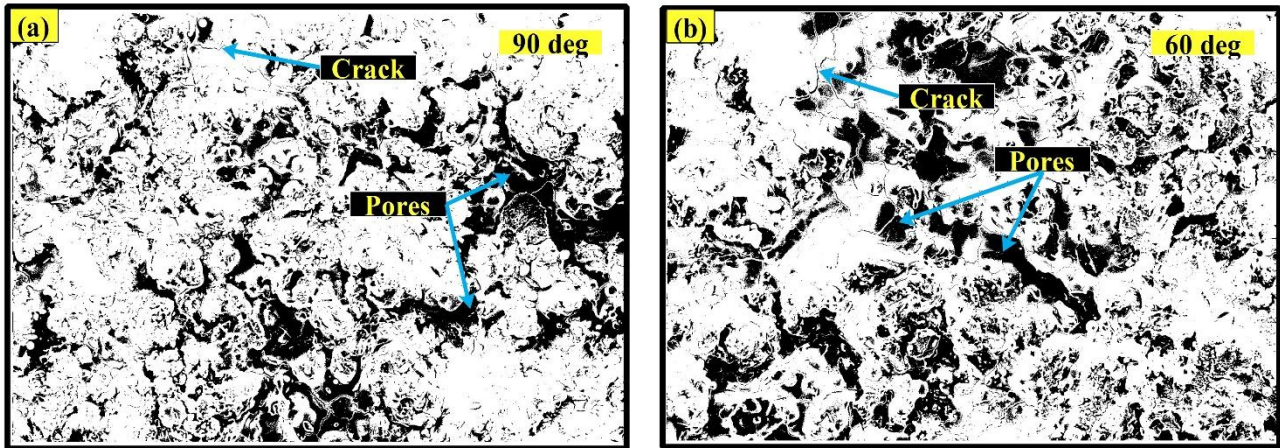


Fig. 13. Surface porosity in plasma sprayed 8YSZ TBCs with spray angles (a) 90° and (b) 60° showing white portion as grain and black portion as pores, cracks, and surface irregularities.

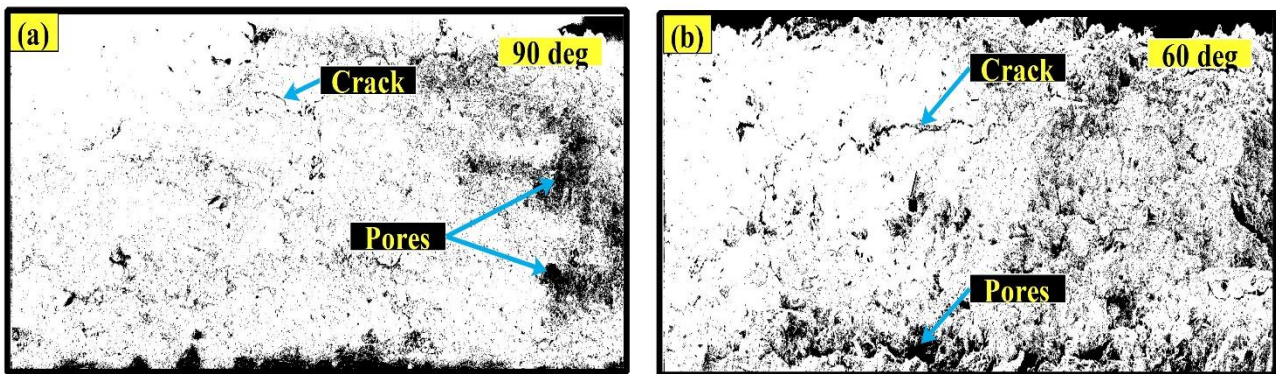


Fig. 14. Cross-sectional surface porosity in plasma sprayed 8YSZ TBCs with spray angles (a) 90° and (b) 60° showing white portion as grain and black portion as pores, cracks, and surface irregularities.

Table 2 and Table 3 show the porosity area and average porosity area of surface and cross-sectional of structure in terms of total area percentage for 8YSZ TBCs with the variation of spray angle conditions. Both TBC samples showed a high amount of porosity with the variation of spray angle conditions. The P60 had a more amount of porous level than P90 TBC. Even defects such as cracks are more visible in P60. The small area of porous structure leads to a low shadow region resulting in better surface roughness. In terms of average porosity, the structured surface P90 shows

$25.11 \pm 0.777\%$ filled with the porous area, the network of cracks, and surface irregularities, whereas P60 showed $29.08 \pm 0.503\%$. The cross-sectional average porosity for P90 is $12.33 \pm 0.608\%$, whereas the P60 showed $19.83 \pm 0.649\%$. In both surface and cross-sectional structures, the P60 TBC results increase in the porosity area compared to P90 TBC with a decrease in spray angle. The spray angle showed the change in the amount of pores, cracks, and surface irregularities. The porosity area in the coating is increased with a decrease in the spray angle [26].

Table 2. Porosity level on the surface structure of plasma sprayed 8YSZ TBCs.

Sample Type	Spray Angle (°)	Surface Porosity (%)	Surface Average Porosity (%)
P90	90	25.57	25.11 ± 0.777 ($\sigma = 0.6861$)
		24.14	
		25.62	
P60	60	28.96	29.08 ± 0.503 ($\sigma = 0.444$)
		28.60	
		29.67	

Table 3. Porosity level in the cross-sectional of plasma sprayed 8YSZ TBCs.

Sample Type	Spray Angle (°)	C/S Porosity (%)	C/S Average Porosity (%)
P90	90	12.41	12.33 ± 0.608 ($\sigma = 0.5375$)
		12.95	
		11.64	
P60	60	19.20	19.83 ± 0.649 ($\sigma = 0.5734$)
		20.59	
		19.72	

3.8 Residual stress

The Raman spectrometer was used to record the spectrum and phases of the coating structure subjected to thermal conditions. First, the coating was heated at 50°C/min until 500°C was achieved. Then, the coating was maintained at the temperature of 500°C for 10mins followed by a holding time of 10mins. Further, the coating was cooled at 50°C/min until it reached the atmospheric temperature of about 27°C. Figure 15 and Figure 16 shows the Raman spectrum, tetragonal and monoclinic phases of 8YSZ TBCs with 90° and 60° spray angle. The typical Raman spectrum for the tetragonal phase of 8YSZ TBCs is 147, 255, 315, 466, and 637cm⁻¹. Therefore, the Raman band spectra region was considered from 150 to 750cm⁻¹, and a peak obtained near 640cm⁻¹ was considered for residual stress analysis due to the better signal-to-noise ratio. The linear relationship between applied stress and peak shift with each cm⁻¹ shift corresponds to 220MPa [22]. The dense coating structure was scanned, and the thermal load was introduced to obtain the Raman band spectra. The Raman shift difference was recorded before and after each 5 thermal cycle interval to measure the induced residual stress during the thermal load in the coating structure.

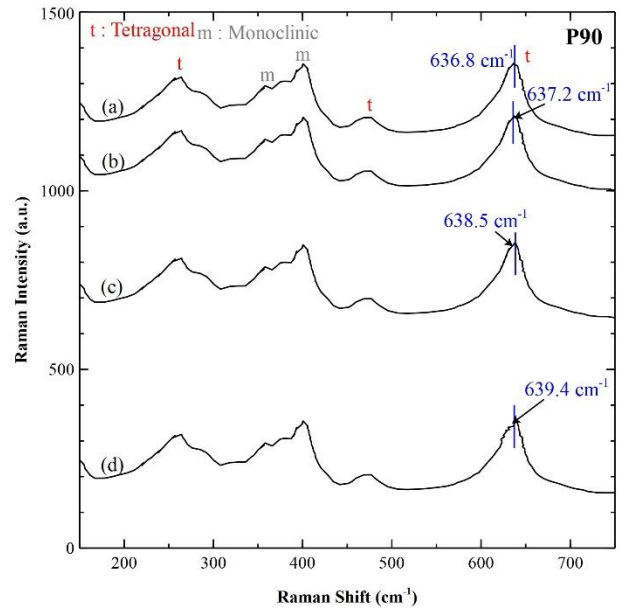
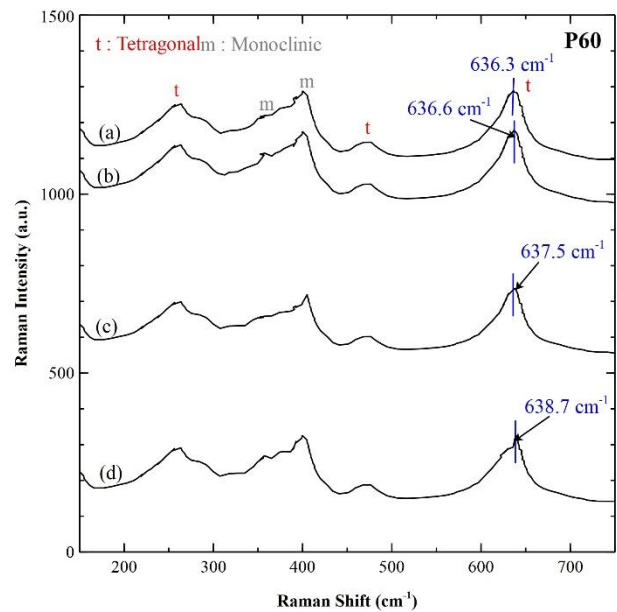
**Fig. 15.** Raman spectrum of P90 TBC (a) as-coated, (b) after 5th, (c) after 10th, and (d) after 15th thermal cycle.**Fig. 16.** Raman spectrum of P60 TBC (a) as-coated, (b) after 5th, (c) after 10th, and (d) after 15th thermal cycle.

Table 4 shows the modes of Raman stretching, the difference of Raman spectrum before and after thermal cycle, average Raman shift with the variation of spray angle. It also showed the compressive residual stresses generated after each interval of 5 thermal cycles. The as-coated P90 TBC showed 636.8 cm⁻¹ Raman spectra whereas P60 TBC showed 636.3 cm⁻¹. After the thermal cycle, the P90 showed more shift in the Raman band compared to P60 TBC. The average Raman shift for P90 is 1.5667±1.022cm⁻¹, whereas for P60 is 1.3±0.973cm⁻¹. During thermal loading, the small

porous structure can result in large compressive residual stresses. It showed that the Raman bands for as-coated were employed in the tetragonal phase of zirconia, and the Raman peak bands were shifted towards low wavenumber. At the 15th thermal cycle, the compressive residual stresses induced in P90 TBC are around 572MPa, whereas P60 TBC is 528MPa. The spray angle affects the porosity, which induces compressive stresses during thermal loading. It means the decrease in spray angle leads to more porosity, resulting in low residual stress-induced.

Table 4. Raman stretching modes, difference before and after thermal cycle, avg. Raman shift and residual stress.

Sample Type and State	Raman Stretching Modes (cm ⁻¹)	Difference before and after thermal cycle (cm ⁻¹)	Avg. Raman Shift (cm ⁻¹)	Residual Stress, σ (MPa)
P90-as coated	636.8	-	1.5667 ± 1.022 ($\sigma = 0.903$)	-
P90-5 th cycle	637.2	0.4		-88
P90-10 th cycle	638.5	1.7		-374
P90-15 th cycle	639.4	2.6		-572
P60-as-coated	636.3	-	1.3 ± 0.973 ($\sigma = 8602$)	-
P60-5 th cycle	636.6	0.3		-66
P60-10 th cycle	637.5	1.2		-264
P60-15 th cycle	638.7	2.4		-528

3.9 Thermal conductivity

Figure 17 shows the thermal conductivity measured with the variation of the spray angle parameter. From Figure 17, both the TBC sample showed high thermal conductivity values at low temperatures and decreased as the temperature is increased. The P90 TBC showed high thermal conductivity than P60 TBC. The thermal conductivity decreases with an increase in the level of porosity. The thermal conductivity varies

between 3.4W/mK and 2.7W/mK with the variation of spray angle conditions at room temperature. At 1000°C, the thermal conductivity of both TBC samples varied between 1.8W/mK and 1.5W/mK.

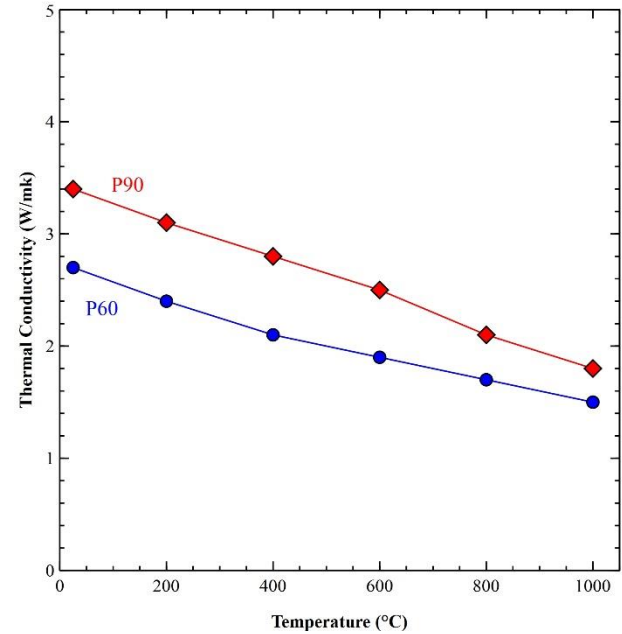


Fig. 17. Thermal conductivity of plasma sprayed 8YSZ TBC with the variation of spray angle.

3.10 Coating hardness

Table 5 and Table 6 represent the surface and cross-sectional hardness value of plasma sprayed 8YSZ TBCs. The effect of spray angle over the coating hardness was measured. The P90 TBC showed a higher value of hardness than P60 TBC as the surface consists of few defects such as cracks and pores contributing to high hardness. The presence of pores and cracks in the coating structure results in low hardness, whereas the better-molten flow of particles with high flatterness leads to high hardness. As P60 had a more porous structure than P90, it contributes to large shadow region results in a low value of hardness. The P90 shows the surface average hardness value of 8.196 ± 0.132 Pa compared to P60, which shows 7.884 ± 0.08 Pa. Whereas on the cross-sectional structure, the P90 showed 8.505 ± 0.224 Pa, and P60 showed 8.004 ± 0.119 Pa. A small amount of increase in the hardness value was observed in normal spray angle compared to inclined spray angle. The spray angle changed the result in a change in coating structure, affecting the coating hardness. The decrease in spray angle condition decreases the value of coating hardness [26].

Table 5. The surface hardness of plasma sprayed 8YSZ TBCs.

Sample Type	Spray Angle (°)	Surface Hardness $\times 10^9$ (Pa)	Surface Average Hardness $\times 10^9$ (Pa)
P90	90	8.103	8.196 ± 0.132 ($\sigma = 0.1503$)
		8.364	
		7.969	
		8.191	
		8.353	
P60	60	7.969	7.884 ± 0.08 ($\sigma = 0.0912$)
		7.802	
		7.761	
		7.996	
		7.890	

Table 6. The cross-sectional hardness of plasma sprayed 8YSZ TBCs.

Sample Type	Spray Angle (°)	C/S Hardness $\times 10^9$ (Pa)	C/S Average Hardness $\times 10^9$ (Pa)
P90	90	8.594	8.505 ± 0.224 ($\sigma = 0.2795$)
		8.629	
		8.152	
		8.697	
		8.854	
P60	60	8.102	8.004 ± 0.119 ($\sigma = 0.1355$)
		7.958	
		7.815	
		8.205	
		7.941	

3.11 Surface roughness

Table 7 represents the surface roughness value of plasma sprayed 8YSZ TBCs. The arithmetic mean roughness (Ra) was determined with the variation of the spray angle parameter. The surface roughness was determined to compare the uniformity of the structure. The defect present in the structure could lead to a rough surface, resulting in poor performance. The rough coating surface in contact with the contour surface could lead to uneven contact resulting in non-uniform wear and uneven temperature drop. Therefore, surface roughness is one of the

important parameters to measure. From Table 7, it can be seen that the P90 structured TBC showed $5.679 \pm 0.141 \mu\text{m}$, whereas the P60 had $7.028 \pm 0.105 \mu\text{m}$. Even the variation in surface roughness was observed more in the case of P60 TBC. The P90 TBC had few defects that result in better microstructural and mechanical properties, whereas P60 had more surface irregularities, resulting in more roughness. A low spray angle than a normal spray angle leads to a rough coating structure with more defects, leading to poor performance [35].

Table 7. The surface roughness of plasma sprayed 8YSZ TBCs.

Sample Type	Spray Angle (°)	Surface Roughness (μm)	Average Surface Roughness (μm)
P90	90	5.734	5.679 ± 0.141 ($\sigma = 0.1760$)
		5.524	
		5.921	
		5.865	
		5.436	
P60	60	5.597	7.028 ± 0.105 ($\sigma = 0.1315$)
		6.864	
		7.126	
		6.954	
		7.059	
		7.249	
		6.918	

4. CONCLUSION

The effect of spray angle onto the plasma sprayed 8YSZ TBC has been studied in the current work. As a result, the surface microstructural characteristics, residual stress, thermal conductivity, and mechanical properties were determined. Based on the experimentation, the following points are drawn:

- The P90 TBC showed a uniform and dense structure, whereas the P60 TBC had a non-uniform and rough surface structure.
- At higher magnification, the P90 showed a small crack width and small crack angle than P60 TBC.
- The P60 TBC had more defects such as cracks, pores, and surface irregularities.

- Both TBC structures showed hexagonal grain boundaries with inter-crystalline space and equiaxed.
- The average grain size for P90 is approx.~ 850nm, whereas P60 is~ 300nm.
- Both TBC showed inter-splat and intra-splat cracks, vertical grain growth structure.
- In terms of avg. porosity, the surface and cross-sectional structure of P60 had more porous area than P90 TBC.
- The avg. Raman shift for P90 is $1.5667 \pm 1.022 \text{ cm}^{-1}$, whereas for P60 is $1.3 \pm 0.973 \text{ cm}^{-1}$.
- The compressive residual stresses induced in P90 and P60 are 572MPa and 528MPa, respectively.
- The change in spray angle leads to variation in thermal conductivity from 3.4W/mK to 2.7W/mK (room temp.) whereas, at 1000°C, it varies from 1.8W/mK to 1.5W/mK.
- The P90 TBC had better hardness and uniform surface roughness than P60 TBC.

Acknowledgment

The experimental work was supported by the Department of Mechanical Engineering, SEM, and Raman spectroscopy by the Central Sophisticated Instrumentation Facility (CSIF), BITS Pilani, K. K. Birla Goa Campus, Goa, India – 403 726.

REFERENCES

- [1] X.Q. Cao, R. Vassen, D. Stoeber, *Ceramic Materials for Thermal Barrier Coatings*, Journal of the European Ceramic Society, vol. 24, iss. 1, pp. 1–10, 2004, doi: [10.1016/S0955-2219\(03\)00129-8](https://doi.org/10.1016/S0955-2219(03)00129-8)
- [2] T.S. Hille, T.J. Nijdam, A.S.J. Suiker, S. Turteltaub, W.G. Sloof, *Damage Growth Triggered by Interface Irregularities in Thermal Barrier Coatings*, Acta Materialia, vol. 57, iss. 9, pp. 2624–2630, 2009, doi: [10.1016/j.actamat.2009.01.022](https://doi.org/10.1016/j.actamat.2009.01.022)
- [3] R. Vaßen, M.O. Jarligo, T. Steinke, D.E. Mack, and D. Stöver, *Overview on Advanced Thermal Barrier Coatings*, Surface and Coatings Technology, vol. 205, iss. 4, pp. 938–942, 2010, doi: [10.1016/j.surfcoat.2010.08.151](https://doi.org/10.1016/j.surfcoat.2010.08.151)
- [4] D. Zhang, Z. Zhao, B. Wang, S. Li, J. Zhang, *Investigation of a New Type of Composite Ceramics for Thermal Barrier Coatings*, Materials and Design, vol. 112, pp. 27–33, 2016, doi: [10.1016/j.matdes.2016.09.050](https://doi.org/10.1016/j.matdes.2016.09.050)
- [5] A.M. Karlsson, *Modelling Failures of Thermal Barrier Coatings*, Key Engineering Materials, vol. 333, pp. 155–166, 2009, doi: [10.4028/www.scientific.net/kem.333.155](https://doi.org/10.4028/www.scientific.net/kem.333.155)
- [6] N.R. Kadam, G. Karthikeyan, D.M. Kulkarni, *Microstructure and Mechanical Properties of Atmospheric Plasma Sprayed 8YSZ Thermal Barrier Coatings*, in M.S. Shunmugam, M. Kanthababu (Ed.): Lecture Notes on Multidisciplinary Industrial Engineering Advances in Micro and Nano Manufacturing and Surface Engineering, Springer, pp. 437–446, 2019, doi: [10.1007/978-981-32-9425-7](https://doi.org/10.1007/978-981-32-9425-7)
- [7] R.C.T. Tucker Jr, *Introduction to Coating Design and Processing*, in Thermal Spray Technology, vol. 5A, ASM Handbook, 2013, pp. 76–88, 2013.
- [8] G. Montavon, S. Sampath, C.C. Berndt, H. Herman, and C. Coddet, *Effects of the Spray Angle on Splat Morphology During Thermal Spraying*, Surface and Coatings Technology, vol. 91, iss. 1–2, pp. 107–115, 1997, doi: [10.1016/S0257-8972\(96\)03137-4](https://doi.org/10.1016/S0257-8972(96)03137-4)
- [9] J. Ilavsky, A.J. Allen, G.G. Long, S. Krueger, C.C. Berndt, H. Herman, *Influence of Spray Angle on the Pore and Crack Microstructure of Plasma-Sprayed Deposits*, Journal of the American Ceramic Society, vol. 80, iss. 3, pp. 733–742, 1997, doi: [10.1111/j.1151-2916.1997.tb02890.x](https://doi.org/10.1111/j.1151-2916.1997.tb02890.x)
- [10] L. Tang, J. Kang, P. He, S. Ding, S. Chen, M. Liu, *Effects of Spraying Conditions on the Microstructure and Properties of NiCrBSi Coatings Prepared by Internal Rotating Plasma Spraying*, Surface and Coatings Technology, vol. 374, pp. 625–633, 2019, doi: [10.1016/j.surfcoat.2019.06.056](https://doi.org/10.1016/j.surfcoat.2019.06.056)
- [11] D. Kumar, K.N. Pandey, *Optimization of the Process Parameters in Generic Thermal Barrier Coatings Using the Taguchi Method and Grey Relational Analysis*, Proceedings of the Institution of Mechanical Engineers, Part L: Journal of Materials: Design and Applications, vol. 231, iss. 7, pp. 600–610, 2017, doi: [10.1177/1464420715602727](https://doi.org/10.1177/1464420715602727)
- [12] S. Mantry, R. Sahoo, B.B. Jha, B.K. Mishra, M. Chakraborty, *Tribo-performance of Plasma-Sprayed Nanostructured Yttria-Stabilized Zirconia Coatings Using Taguchi's Experimental Design*, Proceedings of the Institution of Mechanical Engineers, Part J: Journal of Engineering Tribology, vol. 228, iss. 8, pp. 872–880, 2014, doi: [10.1177/1350650114535385](https://doi.org/10.1177/1350650114535385)
- [13] J.G. Odhiambo, W.G. Li, Y.T. Zhao, C.L. Li, *Porosity and Its Significance in Plasma-Sprayed Coatings*, Coatings, vol. 9, iss. 7, pp. 1–19, 2019, doi: [10.3390/coatings9070460](https://doi.org/10.3390/coatings9070460)
- [14] M.F. Morks, C.C. Berndt, Y. Durandet, M. Brandt, J. Wang, *Microscopic Observation of Laser Glazed Yttria-Stabilized Zirconia Coatings*, Applied Surface Science, vol. 256, iss. 21, pp. 6213–6218, 2010, doi: [10.1016/j.apsusc.2010.03.143](https://doi.org/10.1016/j.apsusc.2010.03.143)

- [15] M. Izadinia, R. Soltani, M.H. Sohi, *Formation of Vertical Cracks in Air Plasma Sprayed YSZ Coatings Using Unpyrolyzed Powder*, Ceramics International, vol. 46, iss. 14, pp. 22383–22390, 2020, doi: [10.1016/j.ceramint.2020.05.320](https://doi.org/10.1016/j.ceramint.2020.05.320)
- [16] H. Nayak, N. Krishnamurthy, R.A. Shailesh, *Studies on Plasma Sprayed Thermal Barrier Coating with Increase in Coating Thickness*, Tribology in Industry, vol. 40, no. 3, pp. 420–432, 2018, doi: [10.24874/ti.2018.40.03.08](https://doi.org/10.24874/ti.2018.40.03.08)
- [17] J. Wang, J. Sun, H. Zhang, S. Dong, J. Jiang, L. Deng, X. Zhou, X. Cao, *Effect of Spraying Power on Microstructure and Property of Nanostructured YSZ Thermal Barrier Coatings*, Journal of Alloys and Compounds, vol. 730, pp. 471–482, 2018, doi: [10.1016/j.jallcom.2017.09.323](https://doi.org/10.1016/j.jallcom.2017.09.323)
- [18] J. Zhu, K. Ma, *Microstructural and Mechanical Properties of Thermal Barrier Coating at 1400°C Treatment*, Theoretical and Applied Mechanics Letters, vol. 4, no. 2, p. 021008, 2014, doi: [10.1063/2.1402108](https://doi.org/10.1063/2.1402108)
- [19] J. Ekberg, A. Ganvir, U. Klement, L. Nordstierna, and U. Klement, *The Influence of Heat Treatments on the Porosity of Suspension Plasma-Sprayed Yttria-Stabilized Zirconia Coatings*, Journal of Thermal Spray Technology, vol. 27, no. 3, pp. 391–401, 2018, doi: [10.1007/s11666-017-0682-y](https://doi.org/10.1007/s11666-017-0682-y)
- [20] X. Zhang, J. Kulczyk-Malecka, J. Carr, P. Xiao, P.J. Withers, *3D Characterization of Porosity in an Air Plasma-Sprayed Thermal Barrier Coating and Its Effect on Thermal Conductivity*, Journal of the American Ceramic Society, vol. 101, iss. 6, pp. 2482–2492, 2018, doi: [10.1111/jace.15409](https://doi.org/10.1111/jace.15409)
- [21] A. Ganvir, N. Markocsan, S. Joshi, *Influence of Isothermal Heat Treatment on Porosity and Crystallite Size in Axial Suspension Plasma Sprayed Thermal Barrier Coatings for Gas Turbine Applications*, Coatings, vol. 7, iss. 1, pp. 1–14, 2016, doi: [10.3390/coatings7010004](https://doi.org/10.3390/coatings7010004)
- [22] V. Teixeira, M. Andritschky, W. Fischer, H.P. Buchkremer, D. Sto, *Analysis of Residual Stresses in Thermal Barrier Coatings*, Journal of Materials Processing Technology, vol. 92–93, pp. 209–216, 1999, doi: [10.1016/S0924-0136\(99\)00157-0](https://doi.org/10.1016/S0924-0136(99)00157-0)
- [23] A. Scrivani, G. Rizzi, U. Bardi, C. Giolli, M.M. Miranda, S. Clattini, A. Fossati, F. Borgioli, *Thermal Fatigue Behavior of Thick and Porous Thermal Barrier Coatings Systems*, Journal of Thermal Spray Technology, vol. 16, iss. 5–6, pp. 816–821, 2007, doi: [10.1007/s11666-007-9128-2](https://doi.org/10.1007/s11666-007-9128-2)
- [24] A. Portinha, V. Teixeira, J. Carneiro, M.G. Beghi, C.E. Bottani, N. Franco, R. Vassen, D. Stoeber, A.D. Sequeira, *Residual Stresses and Elastic Modulus of Thermal Barrier Coatings Graded in Porosity*, Surface and Coatings Technology, vol. 188–189, pp. 120–128, 2004, doi: [10.1016/j.surfcoat.2004.08.014](https://doi.org/10.1016/j.surfcoat.2004.08.014)
- [25] N.R. Kadam, G. Karthikeyan, D.M. Kulkarni, *Effect of Substrate Rotation on the Microstructure of 8YSZ Thermal Barrier Coatings by EB-PVD*, Materials Today: Proceedings, vol. 28, pp. 678–683, 2020, doi: [10.1016/j.matpr.2019.12.276](https://doi.org/10.1016/j.matpr.2019.12.276)
- [26] N.R. Kadam, G. Karthikeyan, D.M. Kulkarni, *Effect of Spray Angle onto the Microstructure of EB-PVD Enabled 8YSZ Thermal Barrier Coatings*, Materials Today: Proceedings, vol. 44, pp. 1111–1117, 2021, doi: [10.1016/j.matpr.2020.11.187](https://doi.org/10.1016/j.matpr.2020.11.187)
- [27] D. Kumar, K.N. Pandey, D.K. Das, *Characterization of Air Plasma Based 7YSZ Aluminum Alloys Thermal Barrier Systems for Hot Zone*, Proceedings of the Institution of Mechanical Engineers, part L: Journal of Materials: Design and Applications, vol. 232, iss. 7, pp. 582–591, 2018, doi: [10.1177/1464420716640570](https://doi.org/10.1177/1464420716640570)
- [28] H. Du, J.H. Shin, S.W. Lee, *Study on Porosity of Plasma-Sprayed Coatings by Digital Image Analysis Method*, Journal of Thermal Spray Technology, vol. 14, iss. 4, pp. 453–461, 2005, doi: [10.1361/105996305X76450](https://doi.org/10.1361/105996305X76450)
- [29] N. Curry, M. Leitner, K. Körner, *High-Porosity Thermal Barrier Coatings from High-Power Plasma Spray Equipment-Processing, Performance and Economics*, Coatings, vol. 10, pp. 1–25, 2020, doi: [10.3390/coatings10100957](https://doi.org/10.3390/coatings10100957)
- [30] W. Tillmann, O. Khalil, M. Abdulgader, *Porosity Characterization and Its Effect on Thermal Properties of APS-Sprayed Alumina Coatings*, Coatings, vol. 9, iss. 10, pp. 601, 2019, doi: [10.3390/coatings9100601](https://doi.org/10.3390/coatings9100601)
- [31] ASTM E1641-11, *Standard Test Method for Thermal Diffusivity by the Flash Method*, 2011, doi: [10.1520/E1461-11](https://doi.org/10.1520/E1461-11)
- [32] ASTM E92-82, *Standard Test Method for Vickers Hardness of Metallic Materials*, 2003, doi: [10.1520/E0092-82R03](https://doi.org/10.1520/E0092-82R03)
- [33] ASTM E384-17, *Standard Test for Method Microindentation Hardness of Materials*, 2017, doi: [10.1520/E0384-17](https://doi.org/10.1520/E0384-17)
- [34] E. Garcia, P. Miranzo, R. Soltani, T.W. Coyle, *Microstructure and Thermal Behavior of Thermal Barrier Coatings*, Journal of Thermal Spray Technology, vol. 17, iss. 4, pp. 478–485, 2008, doi: [10.1007/s11666-008-9200-6](https://doi.org/10.1007/s11666-008-9200-6)
- [35] N.R. Kadam, G. Karthikeyan, D.M. Kulkarni, *The Effect of spray angle on the microstructural and mechanical properties of plasma sprayed 8YSZ Thermal Barrier Coatings*, Journal of Micromanufacturing, pp. 1–12, 2021, doi: [10.1177/25165984211016323](https://doi.org/10.1177/25165984211016323)